Catalan solids from superionic nanoparticles

Tong Bian[1], Ivan Lobato[2], Ji Wang[1], Tara A. Nitka[3], Tzuf Shay Peled[1], Byeongdu Lee[4], Sandra Van Aert[2], Sara Bals[2], Lela Vuković[3], Thomas Altantzis[2]*, Petr Král[5]* & Rafal Klajn[1]*

[1]Department of Organic Chemistry, Weizmann Institute of Science, Rehovot 76100, Israel
[2]Electron Microscopy for Materials Science (EMAT), University of Antwerp, Antwerp 2020, Belgium
[3]Department of Chemistry and Biochemistry, University of Texas, El Paso, TX 79966, USA
[4]X-Ray Science Division, Argonne National Laboratory, Argonne, IL 60439, USA
[5]Departments of Chemistry, Physics, and Biopharmaceutical Sciences, University of Illinois, Chicago, IL 60607, USA

*e-mail: rafal.klajn@weizmann.ac.il; pkral@uic.edu; thomas.altantzis@uantwerpen.be

The self-assembly of inorganic nanoparticles (NPs) into ordered structures (superlattices)[1] has led to a wide range of nanomaterials with unique optical,[2,3] magnetic,[4] electronic,[5] and catalytic[6,7] properties. Various interactions[8] have been employed to direct the crystallization of NPs, including van der Waals forces,[9,10] hydrogen bonding,[11-13] as well as electric[14] and magnetic[15] dipolar interactions. Among them, Coulombic interactions—ubiquitous in nature[16,17] and the main driving force behind the formation of many minerals, such as fluorite or rock salt—have remained largely underexplored,[18,19] owing to the rapid charge exchange[19] between NPs bearing high densities of opposite charges (superionic NPs). Here, we worked with superionic NPs under conditions (room temperature, concentrated salt solutions) that preserved their native surface charge density. We demonstrate that under these conditions, the Coulombic interactions between superionic NPs are reminiscent of short-range intermolecular interactions. Our methodology was used to assemble oppositely charged NPs into high-quality superlattices exhibiting Catalan shapes. Depending on their size ratio, the NPs assembled into either rhombic dodecahedra or triakis tetrahedra with structures mimicking those of the ionic solids CsCl and Th_3P_4, respectively. We envision that the methodology described here can be applied to a wide range of charged NPs of various sizes, shapes, and compositions, thus facilitating the discovery of new nanomaterials.

Charged NPs have long been known[20-24] and Coulombic interactions between oppositely charged NPs[18,19] have been investigated. Noble metal NPs decorated with monolayers of thiolate ligands terminated with charged groups can accommodate up to ~2 charges per nm^2. Such densely charged NPs can mimic the behaviors of small ions on a nanometer scale; we thus refer to them as superionic nanoparticles. In a

pioneering study,[18] equally sized positively and negatively charged gold NPs were coassembled into colloidal crystals with a structure mimicking that of sphalerite ($M^{2+}S^{2-}$, where M = Zn and Fe). However, it was subsequently demonstrated[19] that the process, which occurred at 70 ºC, involved a substantial degree of thiolate-ligand exchange between the positively and negatively charged NPs, affording two populations of zwitterionic NPs:[19,25-27] one having a small excess of positive charge and the other, a small excess of negative charge (in fact, thiolates on gold are labile and can readily desorb at temperatures exceeding 60 ºC[28-30]). An alternative approach to provide inorganic NPs with electric charge is to encapsulate them within charged protein cages.[31] Although crystalline assemblies of protein-encapsulated NPs have been obtained,[32,33] this method suffers from a relatively low charge density on the protein surface. Therefore, assemblies resulting from electrostatic interactions between heavily charged NPs—in particular, superionic NPs—have remained unknown.

We worked with monodisperse gold NPs with >20 distinct sizes varying between 2.6 and 8.5 nm (the size refers to the diameter of the NP's metallic core). These NPs were synthesized in toluene in the presence of oleylamine (OLA) as the capping ligand. To endow Au·OLA NPs with negative and positive surface charges, we performed a ligand exchange reaction, in which the weakly binding OLA was replaced with strongly bound thiols: 11-mercaptoundecanoate (MUA) and (11-mercaptoundecyl)-*N*,*N*,*N*-trimethylammonium (TMA), respectively (Fig. 1a, bottom). Au NPs functionalized with a single-component monolayer of MUA (i.e., Au·MUA) exhibited excellent solubility in basic water (pH=11) for all NP sizes studied. To render Au·TMA soluble in water, a small amount of a short, electrically neutral thiol (we used hexanethiol; ~20 mol%) was included during the ligand exchange (TMA alone proved to be unable to displace all the OLA ligands, even when used in excess). Both Au·MUA and Au·TMA bear hundreds of electric charges (estimated at ~370 negatively and ~290 positively charged groups for Au·MUA and Au·TMA for a typical NP size of 5 nm), with charge densities far exceeding those in both natural[34,35] and artificially supercharged[36-38] proteins.

We began our experiments with mixtures of equally sized Au·MUA and Au·TMA. The pH was adjusted to 11 to ensure complete deprotonation of MUA's terminal COOH groups. Upon mixing aqueous solutions of these two types of NPs, we observed the rapid formation of an amorphous precipitate (stage **1** in Fig. 1a). We hypothesized that ordered assemblies of these superionic NPs could be obtained by gradually increasing the strength of electrostatic interactions (Fig. 1b). To this end, we first established that the Coulombic interactions between Au·MUA and Au·TMA could be screened—and their aggregates disassembled—upon adding concentrated solutions of simple inorganic salts. Among the many salts that

successfully disassembled the Au·MUA/Au·TMA aggregates, we focused on ammonium carbonate, which has the unique ability to spontaneously decompose into gaseous products,[39,40] according to the reaction equation,

$$2\ NH_4^+ + CO_3^{2-} \rightarrow 2\ NH_3 \uparrow + CO_2 \uparrow + H_2O.$$

Indeed, after a colloidally stable solution of Au·MUA + Au·TMA in saturated aqueous $(NH_4)_2CO_3$ (Fig. 1a, stage **2**) was left undisturbed overnight, well-defined and highly faceted colloidal crystals (superlattices) were observed (Fig. 1a, stage **3**). Importantly, all the steps proceeded at room temperature, which allowed the NPs to retain their high charge. We adopted this procedure to ~200 combinations of positively and negatively charged NPs and identified two distinct phases of colloidal crystals, which are mapped onto the phase diagram in Fig. 1c. We will begin the discussion with crystals obtained from equally or similarly sized Au·MUA and Au·TMA; the stoichiometry of these crystals is 1:1; we will refer to them as AB-type.

First, we used the above method to coassemble identically sized (i.e., obtained from the same batch of Au·OLA), 4.83 nm Au·MUA and Au·TMA. Inspection of the resulting black precipitate by scanning electron microscopy (SEM) revealed that the NPs coassembled, in a near-quantitative fashion, into colloidal crystals with a rhombic dodecahedron (RD) morphology (Fig. 2a–c), each bound by 12 identical (110) crystal facets. The average edge length of these crystals is 1.2 μm, meaning that each RD is composed of approximately 10 million individual NPs. The crystals are large enough to be imaged by a benchtop optical microscope (Fig. 2a, inset). The procedure is readily scalable and can be used to prepare multimilligram quantities of RDs in a single experiment. Small-angle X-ray scattering (SAXS) experiments showed that the NPs are arranged in a body-centered cubic lattice (Fig. 2d); i.e., the packing of oppositely charged superions within RDs mimics that of Cs^+ and Cl^- in the crystal lattice of cesium chloride.

The formation of RDs in our system may appear surprising, given that the NPs interact predominantly by electrostatic forces. RD-shaped colloidal crystals with the CsCl structure were previously observed in binary mixtures of NPs interacting via local, highly specific intermolecular interactions (between complementary DNA chains[41-43] and a synthetic hydrogen-bond donor–acceptor pair[44,45]). Although electrostatic interactions are typically long-range, we note that self-assembly in our system occurs in a concentrated salt solution. In fact, we experimentally determined that oppositely charged 5.28 nm NPs initially immersed in a saturated (~10.5 M) $(NH_4)_2CO_3$ solution begin to interact when the concentration

of the evaporating salt is still very high, at ~4.28 M (i.e., at this salt concentration, the NH_4^+ and CO_3^{2-} ions can no longer screen out the Coulombic attraction between oppositely charged NPs). Next, we performed atomistic molecular dynamics (MD) simulations of pairs of oppositely charged (Fig. 1d) and like-charged NPs (Supplementary Fig. 15) in a 4.28 M $(NH_4)_2CO_3$ solution. In such an environment, the Debye screening length is very short ($\lambda \approx 0.1$ nm) and the NPs interact only locally by screened Coulomb coupling between the charged tips of their ligands (i.e., a surface-centered Yukawa-type interaction). Indeed, the free energies of interparticle interactions calculated by an umbrella sampling technique (for details, see Supplementary Section 3) show that the NPs do not experience attractive or repulsive interactions unless they are in close contact (Fig. 1e). For a pair of oppositely charged NPs, the interaction energy increases rapidly from ~0 to –50 kcal/mol over a distance of only ~0.7 nm (Fig. 1e, green trace). Analogously, like-charged NPs couple via sharp repulsive potentials, but not before their ligands are practically in direct contact (within ~0.3 nm of each other) (red and blue traces in Fig. 1e; note that TMA is slightly longer than MUA). Overall, these simulations indicate that electrostatic interactions between superionic NPs at high ionic strengths resemble (in terms of range) specific intermolecular interactions.

To further confirm the structure of RDs, we developed a new method to determine NP packing on a single-aggregate level directly from electron microscopy. The key steps of the procedure are summarized in Fig. 3. First, we acquired a series of high-angle annular dark-field scanning transmission electron microscopy (HAADF-STEM) images over a wide range of tilt angles (–70º to +72º), focusing on a tip of a colloidal crystal (Fig. 3a). After aligning the tilt series, we reconstructed the volume of the imaged region (Fig. 3b) and calculated the corresponding 3D Fourier transform (Fig. 3c). Optimization of the reciprocal vectors (for details, see Supplementary Section 5) followed by inverse Fourier transformation led to a primitive unit cell representative of the entire imaged region. Then, the primitive unit cell was replicated in all directions and overlaid on the reconstructed volume (Fig. 3d). Finally, the second optimization process afforded the complete unit cell (Fig. 3e). We note that whereas the shape of the unit cell determined using the above procedure matched that elucidated by SAXS (α, β, γ = 88.8±2.1º and 90º, respectively; Fig. 3f), the cell's edge length decreased significantly (a, b, c = 7.93±0.03 nm vs. 9.40 nm for SAXS), which can be attributed to drying-induced collapse (40% volume loss) (see also Supplementary Fig. 8).

High-quality RDs were successfully prepared from other mixtures of equally sized Au·MUA and Au·TMA, in the range 3.7–7.4 nm (Fig. 1c). Oppositely charged NPs whose Au cores were smaller than 3.7 nm assembled into spherical aggregates that lacked crystalline order (Supplementary Fig. 5a). When the particles were larger than 7.4 nm, the Coulombic forces between them were so strong and they could

not be screened in saturated $(NH_4)_2CO_3$ solution – i.e., in this size regime, the initial amorphous aggregates (**1** in Fig. 1a) could not be converted into crystalline ones.

The above analysis of interparticle interactions (Fig. 1e) suggests that the assembly process is driven predominantly by short-range electrostatic interactions between NP-adsorbed ligands, with negligible contributions from the van der Waals interactions between the NP cores. To verify this hypothesis, we synthesized positively charged palladium NPs (Pd·TMA) and studied their interactions with similarly sized Au·MUA. The bimetallic Au/Pd RDs (Fig. 2f) were formed similarly to the all-Au RDs, and the two kinds of RDs were indistinguishable by SEM; however, elemental analysis revealed the expected 1:1 ratio of Au and Pd (Supplementary Fig. 12). By controllably removing the monolayers of organic ligands from the NPs,[3] such mixed crystals could be transformed into new nanostructured materials, in which the nanoscopic domains of two metals alternate.[46]

Next, we worked with mixtures of differently sized Au·MUA and Au·TMA, i.e., outside the diagonal line in Fig. 1c. We found that NP combinations that afforded well-defined RDs span a relatively large region of the phase diagram (see the green markers in Fig. 1c); for example, a mixture of 5.78 nm Au·TMA and 4.19 nm Au·MUA afforded RDs in a near-quantitative yield. This is an interesting finding given that these RDs are built from equal numbers of differently sized Au·MUA and Au·TMA, while the electroneutrality condition implies that the overall number of positive and negative charges within the crystals is the same. Assuming that both MUA and TMA occupy the same surface area on the NP, and that the positive charge on Au·TMA is diluted by an electrically neutral ligand (~34 mol%), it follows from simple geometric considerations that the TMA/MUA molar ratio within these RDs is as high as ~1.25. Next, assuming that the footprint of a thiolate ligand on a gold NP[47] corresponds to 0.22 nm^2 and that all MUA ligands are deprotonated (the pH at the onset of crystallization ≈ 9.2) leads to the conclusion that each Au·MUA/Au·TMA pair has to be accompanied by ~33 CO_3^{2-} ions to compensate for the excess of the positively charged TMA ligands. Similarly, RDs obtained from larger Au·MUAs and smaller Au·TMAs must trap NH_4^+ ions from the surrounding solution as they form in order for electroneutrality to be met. In other words, $(NH_4)_2CO_3$ acts like a "buffer", guiding the formation of colloidal crystals by providing them with small anions or cations to electrically balance the charge-mismatched NPs. Trapping of NH_4^+ and/or CO_3^{2-} by superionic NPs is not unexpected given that the ratio of small ions to NPs at the onset of self-assembly is on the order of 10^7 (see also Supplementary Fig. 11).

The rhombic dodecahedron is an example of a Catalan solid: it is an isohedral (i.e., all faces are the same) yet a non-isogonal (at least two types of vertices) polyhedron, whose faces are not regular

polygons.[48] As noted above, RDs form over a relatively broad range of NP size ratios, but up to a certain limit. When the size ratio of the oppositely charged NPs was increased further, they coassembled into colloidal crystals having the shape of another Catalan solid, namely, the triakis tetrahedron (TT) (Fig. 4a, b). Well-defined TTs were obtained from more than 40 combinations of differently sized Au·MUAs and Au·TMAs, indicated by the orange triangles in Fig. 1c. TTs found on the opposite sides of the diagonal line in the phase diagram were indistinguishable from one another.

SAXS analysis showed (Fig. 4c) that TTs have a cubic symmetry with space group $I\bar{4}3d$, i.e., they are isostructural with Th_3P_4. The Th_3P_4 unit cell is highly complex and contains 35 atoms/particles, resulting in the unit cell having a large size; e.g., for TTs coassembled from 5.63 nm Au·TMA and 3.73 nm Au·MUA, we found (by SAXS) a unit cell edge length of 20.53 nm. Similar to RDs, TTs were bound by a single type of crystal facet, with the Miller index (211). High-resolution SEM imaging revealed a complex pattern of NPs on the faces of TTs (Fig. 4d, e and Supplementary Fig. 13) – another manifestation of the complexity of the unit cell. Interestingly, whereas Th_3P_4-like packing in NP superlattices has been reported,[13,49,50] their morphology (crystal habit) has remained unknown. Notably, the previously reported Th_3P_4-type superlattices were all coassembled from NPs decorated with hydrogen-bond donors and acceptors, which extends the analogy between highly specific noncovalent interactions and the short-range electrostatic interactions operating in our system.

We also attempted to determine the structure of our TTs using the new method outlined in Fig. 2. Analysis of the dried sample revealed that the dimensions of the unit cell decreased, as expected (a, b, c = 16.36±0.26 nm; compare with a, b, c = 20.53 nm for an aqueous suspension of the same TTs, determined from SAXS). Interestingly, the collapse did not appreciably affect the shape of the primitive unit cell (α, β, γ = 89.9±1.1° vs. α, β, γ = 90° from SAXS), despite a significant volume loss of 49%. However, the NPs residing inside the unit cell were significantly disordered upon drying (Supplementary Section 5.2) and of the expected 35 particles per unit cell, we managed to resolve only 33. This finding is not unexpected; we note that evaporation of water and in particular removal of the trapped ions (NH_4^+ and CO_3^{2-}; in the form of NH_3 and CO_2) unscreens the electrostatic interactions between the NPs; hence, the particles will tend to adjust their positions within the crystals so as to minimize the free energy originating from the unscreened interactions between the NPs.

We developed two modeling approaches to rationalize the formation of the experimentally observed lattices from differently sized NP building blocks. First, we constructed a simple geometric model based on varying the sizes of NPs arranged in a given lattice (AB and A_3B_4), where the NPs interact via contact

potentials. According to this model, a lattice will be stable only if oppositely charged NPs are in direct contact; when the NP sizes are such that the oppositely charged NPs cannot be in contact (due to geometric constraints), another lattice will form in which the NPs can regain favorable contacts. It follows from geometric considerations (Supplementary Section 6.1) that the CsCl-type and Th_3P_4-type lattices will fail to form when the size ratio of the oppositely charged NPs is greater than ~1.37 and ~2.08, respectively. These considerations suggest that the Th_3P_4-type lattice should be stable over a relatively large range of NP size ratios, which is in qualitative agreement with the experimental findings (Supplementary Fig. 28). In the second approach, we calculated the free energies of the two lattices by summing the attractive and repulsive interaction energies between the constituent NPs (the interparticle interaction energies were determined from atomistic MD simulations and up/downscaled according to the NP size; for further details on this hybrid approach, see Supplementary Section 6.2). The resulting free-energy maps are shown in Supplementary Fig. 29; these results were then integrated onto a single phase diagram (Fig. 1c), where the regions showing the favorable existence of the CsCl-type and the Th_3P_4-type lattices are highlighted in green and orange, respectively; a reasonable agreement with the experimental data points can be seen.

Finally, it is important to confirm that Au·TMA and Au·MUA retain their identity during self-assembly experiments – i.e., no ligand hopping between the two types of NPs takes place to a significant extent at room temperature. To this end, we performed a series of gel electrophoresis experiments on Au·TMA and Au·MUA with a typical size of 4.83 nm (Supplementary Section 7). In the key experiment, we titrated Au·TMA with Au·MUA, collected the resulting precipitate, redissolved it in a concentrated $(NH_4)_2CO_3$ solution, and allowed the NPs to move in an electric field. We were pleased to find that the mixture of NPs was separated into two bands migrating in opposite directions (Supplementary Fig. 30). Importantly, the two bands travelled the same distance as Au·TMA with Au·MUA, which had not been in contact with the oppositely charged NP. As a control experiment, we heated the Au·TMA/Au·MUA precipitate at 70 ºC, which induced ligand hopping between the NPs, affording a single NP type, i.e., Au·(TMA/MUA). The net charge of these NPs approached zero; hence, they did not migrate in an electric field. The methodology described here is general; we expect that when applied to mixtures of charged NPs of various sizes, shapes, and core compositions, it will lead to a wide range of new nanostructured materials.

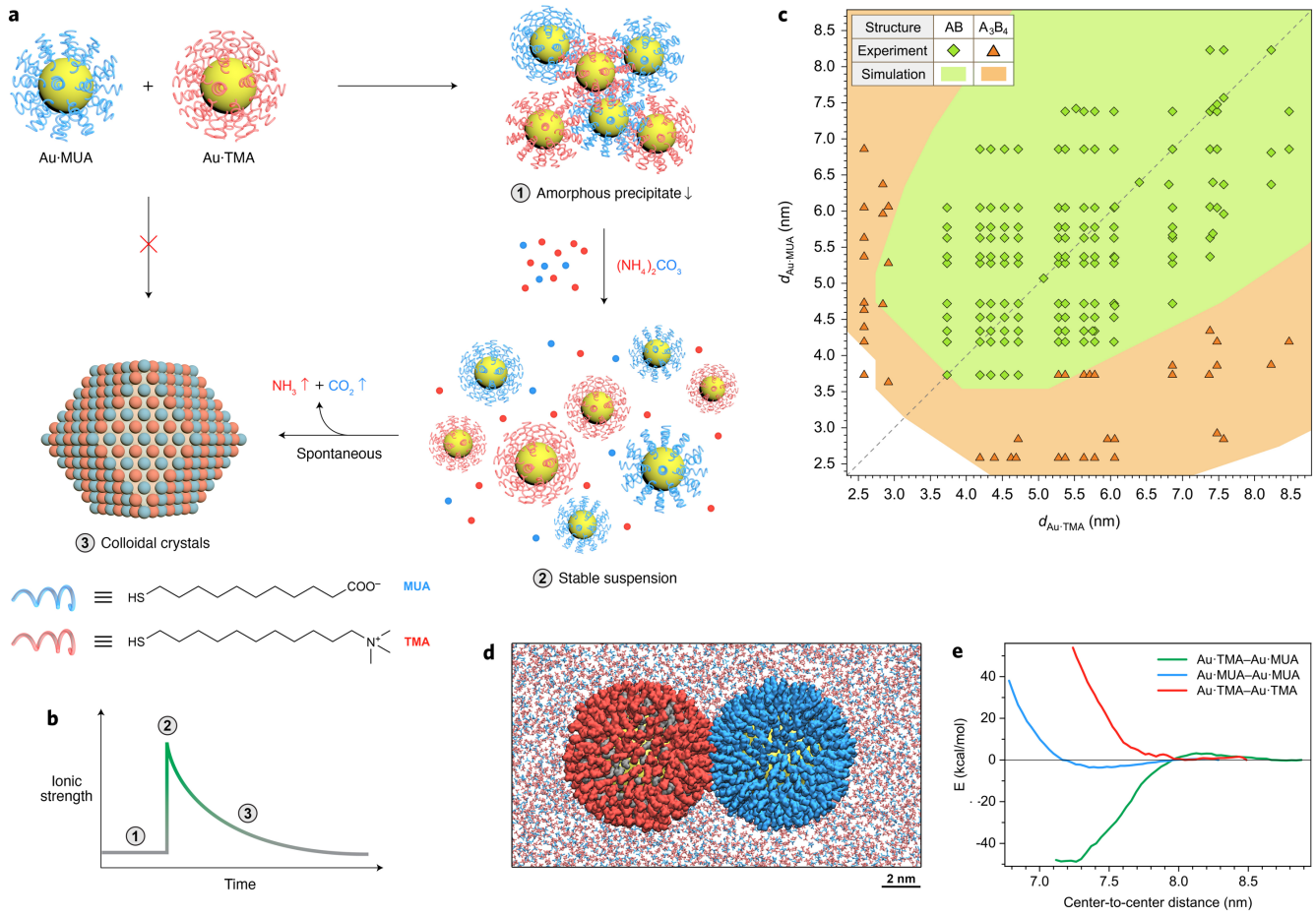

Fig. 1 Colloidal crystals from superionic nanoparticles. a, Schematic representation of the co-crystallization of oppositely charged nanoparticles (NPs) coupled to the evaporation of $(NH_4)_2CO_3$. *Bottom:* Structural formulas of thiols used to provide the NPs with a negative (MUA) and positive (TMA) charge. **b,** Schematic illustration of the change in the ionic strength throughout the process. **c,** Phase diagram of the experimentally observed NP superlattices obtained from ~200 different combinations of MUA- and TMA-coated Au NPs (markers) and their existence regions obtained by computational modeling (the colored regions correspond to energy minima lower than –200 kcal/mol for the AB-type lattice and –150 kcal/mol for the Th_3P_4-type lattice; for details, see Supplementary Section 6.2). **d,** Snapshot from an atomistic simulation of two oppositely charged 5 nm Au NPs immersed in a concentrated (4.28 M) solution of $(NH_4)_2CO_3$ (MUA, blue; TMA, red; hexanethiol, gray; Au core, yellow; NH_4^+, red; CO_3^{2-}, blue; water molecules were omitted for clarity). **e,** Free energies of binding between different pairs of 5 nm NPs, calculated by an umbrella sampling technique (note that each NP is coated with a ~1.5 nm-thick monolayer of TMA/MUA, giving rise to an effective diameter of ~8 nm).

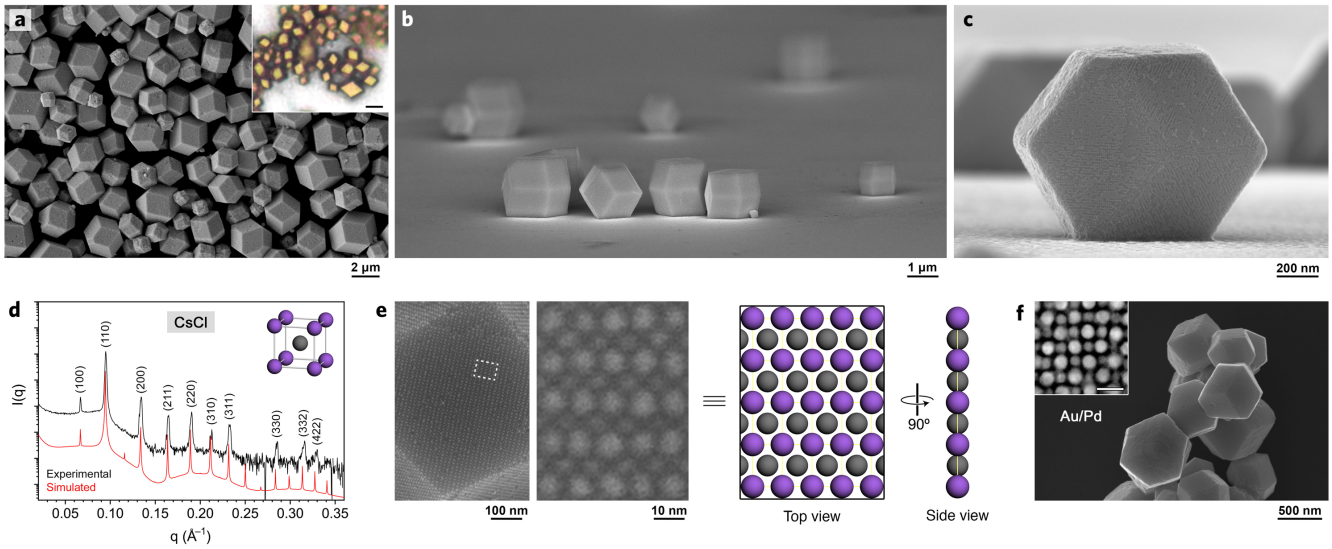

Fig. 2 AB-type colloidal crystals. a, SEM image of AB-type crystals with the shape of a rhombic dodecahedron (RD), coassembled from equally sized, 4.83 nm Au·TMA and Au·MUA. The inset shows an optical micrograph (scale bar = 2 μm). **b,** Side-view SEM image of RDs coassembled from equally sized, 5.28 nm Au·TMA and Au·MUA. **c,** Side-view SEM image of a single RD (coassembled from equally sized, 7.42 nm Au·TMA and Au·MUA). **d**, 1D small-angle X-ray scattering (SAXS) pattern for the AB-type assemblies (black) and a simulated pattern for the CsCl structure (red). SAXS data are represented by plots of scattered intensity I(q) (y-axis, arbitrary units) vs. scattering vector q (x-axis, $Å^{-1}$). **e,** *Left:* SEM images (at two different magnifications) of a (110) facet of a RD (coassembled from 8.23 nm Au·TMA and 6.37 Au·MUA). *Right:* Model of NP packing within the RD's (110) facet, with oppositely charged NPs denoted in purple and gray. **f,** SEM image of RDs coassembled from 4.15 nm Pd·TMA and 5.37 nm Au·MUA. *Inset:* Transmission electron microscopy (TEM) image of an ensemble of 5.07 nm Au·TMA and 3.90 nm Pd·MUA (scale bar = 10 nm).

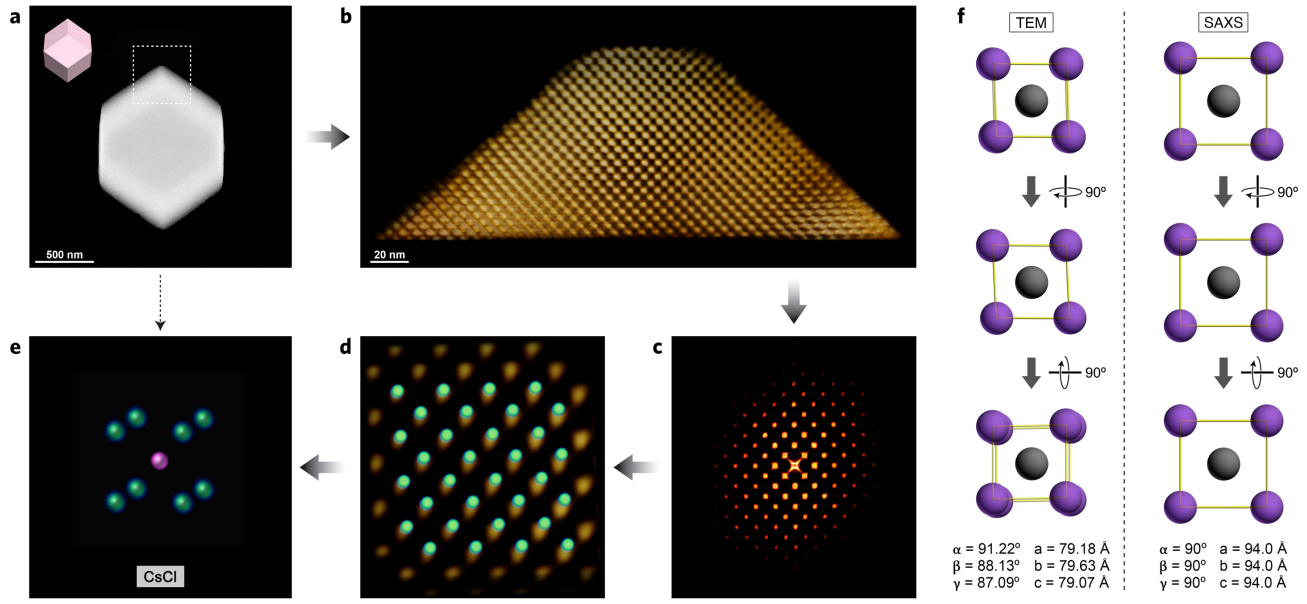

Fig. 3 Procedure developed for determining the unit cell of colloidal crystals from TEM imaging. a, High-angle annular dark-field scanning transmission electron microscopy (HAADF-STEM) image of a single RD. The region denoted by the white frame was used for acquiring the electron tomography series. **b,** 3D reconstructed volume of the region highlighted in (a). **c,** A 3D Fourier transform pattern obtained from the reconstructed volume. **d,** Overlay of the unit cell (green; replicated 3.5 times in all directions) on the reconstructed volume (yellow). **e,** Average unit cell determined after an optimization procedure (for details, see Supplementary Section 5). **f,** Comparison of unit cells of RDs (obtained from equally sized, 5.28 nm Au·TMA and Au·MUA) determined from STEM tomography (left; individual RD in the dry state) and SAXS measurements (right; suspension of RDs in water).

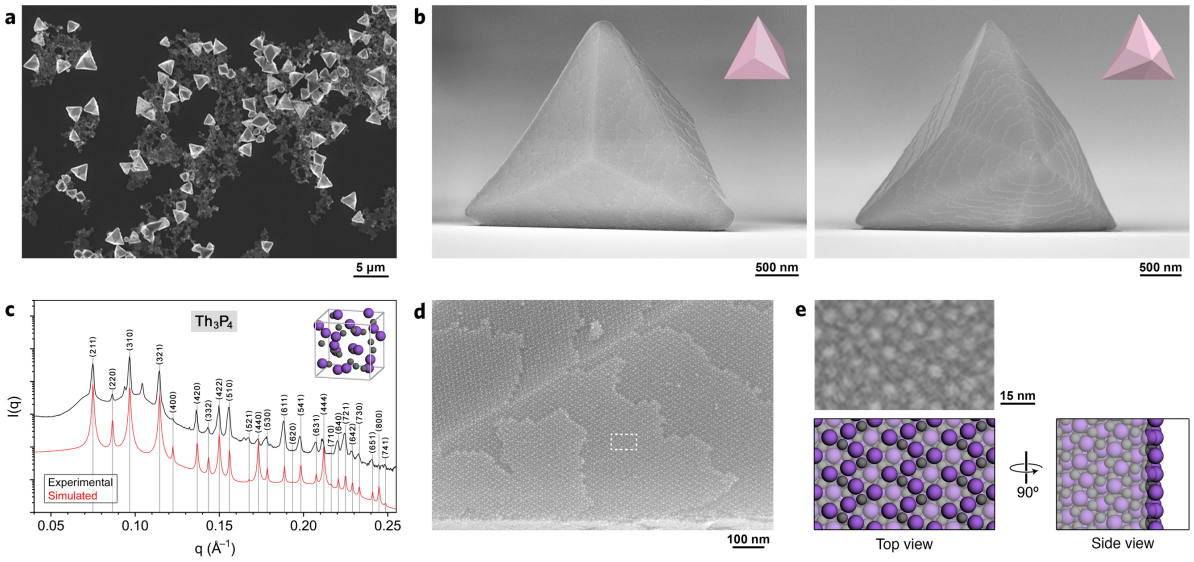

Fig. 4 A_3B_4-type colloidal crystals. a, SEM image of A_3B_4-type crystals with the shape of a triakis tetrahedron (TT), coassembled from 2.92 nm Au·TMA and 5.28 nm Au·MUA. **b,** Side-view SEM images of two TTs viewed along different directions (building blocks: 5.28 nm Au·TMA and 3.73 nm Au·MUA). **c**, SAXS pattern for the A_3B_4-type assemblies (coassembed from 5.63 nm Au·TMA and 3.73 nm Au·MUA) (black) and a simulated pattern for the Th_3P_4 structure (red). **d,** High-resolution SEM image showing the complex packing of NPs comprising the (211) face of a triakis tetrahedron (building blocks: 6.86 nm Au·TMA and 4.39 nm Au·MUA. **e,** *Top:* Magnified view of the region highlighted in (d); *bottom:* Model of NP packing within the TT's (211) facet, with the top layer of the NPs highlighted.

Acknowledgments. We acknowledge funding from the European Union's Horizon 2020 research and innovation program under the European Research Council (ERC) (grants 770887, 815128, and 820008) and the Minerva Foundation with funding from the Federal German Ministry for Education and Research. We acknowledge computer time provided by the Texas Advanced Computing Center (TACC). This research used resources of the Advanced Photon Source, a U.S. Department of Energy (DOE) Office of Science User Facility, operated for the DOE Office of Science by Argonne National Laboratory under Contract No. DE-AC02-06CH11357. Extraordinary facility operations were supported in part by the DOE Office of Science through the National Virtual Biotechnology Laboratory, a consortium of DOE national laboratories focused on the response to COVID-19, with funding provided by the Coronavirus CARES Act.

References

1. Boles, M. A., Engel, M. & Talapin, D. V. Self-assembly of colloidal nanocrystals: From intricate structures to functional materials. *Chem. Rev.* **116**, 11220–11289 (2016).
2. Klinkova, A., Choueiri, R. M. & Kumacheva, E. Self-assembled plasmonic nanostructures. *Chem. Soc. Rev.* **43**, 3976–3991 (2014).
3. Udayabhaskararao, T. et al. Tunable porous nanoallotropes prepared by post-assembly etching of binary nanoparticle superlattices. *Science* **358**, 514–518 (2017).
4. Chen, J. et al. Collective dipolar interactions in self-assembled magnetic binary nanocrystal superlattice membranes. *Nano Lett.* **10**, 5103–5108 (2010).

5. Urban, J. J., Talapin, D. V., Shevchenko, E. V., Kagan, C. R. & Murray, C. B. Synergismin binary nanocrystal superlattices leads to enhanced p-type conductivity in self-assembled PbTe/Ag_2Te thin films. *Nat. Mater.* **6**, 115–121 (2007).
6. Kang, Y. et al. Design of Pt–Pd binary superlattices exploiting shape effects and synergistic effects for oxygen Reduction Reactions. *J. Am. Chem. Soc.* **135**, 42–45 (2013).
7. Lach, M., Künzle, M. & Beck, T. Free-standing metal oxide nanoparticle superlattices constructed with engineered protein containers show in crystallo catalytic activity. *Chem. Eur. J.* **23**, 17482–17486 (2017).
8. Silvera Batista, C. A., Larson, R. G. & Kotov, N. A. Nonadditivity of nanoparticle interactions. *Science* **350**, 1242477 (2015).
9. Bigioni, T. P. et al. Kinetically driven self assembly of highly ordered nanoparticle monolayers. *Nat. Mater.* **5**, 265–270 (2006).
10. Zhuang, J., Wu, H., Yang, Y. & Cao, Y. C. Supercrystalline colloidal particles from artificial atoms. *J. Am. Chem. Soc.* **129**, 14166–14167 (2007).
11. Macfarlane, R. J. et al. Nanoparticle superlattice engineering with DNA. *Science* **334**, 204–208 (2011).
12. Nykypanchuk, D., Maye, M. M., van der Lelie, D. & Gang, O. DNA-guided crystallization of colloidal nanoparticles. *Nature* **451**, 549–552 (2008).
13. Santos, P. J., Cao, Z., Zhang, J., Alexander-Katz, A. & Macfarlane, R. J. Dictating nanoparticle assembly via systems-level control of molecular multivalency. *J. Am. Chem. Soc.* **141**, 14624–14632 (2019).
14. Zhao, H. et al. Reversible trapping and reaction acceleration within dynamically self-assembling nanoflasks. *Nat. Nanotechnol.* **11**, 82–88 (2016).
15. Kapuscinski, M. et al. Temporal evolution of superlattice contraction and defect-induced strain anisotropy in mesocrystals during nanocube self-assembly. *ACS Nano* **14**, 5337–5347 (2020).
16. Thornton, J. M. Electrostatic interactions in proteins. *Nature* **295**, 13–14 (1982).
17. Kornyshev, A. A. & Leikin, S. Electrostatic interaction between helical macromolecules in dense aggregates: An impetus for DNA poly- and mesomorphism. *Proc. Natl. Acad. Sci. USA* **95**, 13579–13584 (1998).
18. Kalsin, A. M. et al. Electrostatic self-assembly of binary nanoparticle crystals with a diamond-like lattice. *Science* **312**, 420–424 (2006).
19. Wang, L., Albouy, P.-A. & Pileni, M.-P. Synthesis and self-assembly behavior of charged Au nanocrystals in aqueous solution. *Chem. Mater.* **27**, 4431–4440 (2015).
20. Kalsin, A. M., Kowalczyk, B., Smoukov, S. K., Klajn, R. & Grzybowski, B. A. Ionic-like behavior of oppositely charged nanoparticles. *J. Am. Chem. Soc.* **128**, 15046–15047 (2006).
21. Hassinen, J., Liljeström, V., Kostiainen, M. A. & Ras, R. H. A. Rapid cationization of gold nanoparticles by two-step phase transfer. *Angew. Chem. Int. Ed.* **54**, 7990–7993 (2015).
22. Zhang, H., Muhammad, J., Liu, K., Ras, R. H. A. & Ikkala, O. Light-induced reversible hydrophobization of cationic gold nanoparticles via electrostatic adsorption of a photoacid. *Nanoscale* **11**, 14118–14122 (2019).
23. Rao, A. et al. Regulation of interparticle forces reveals controlled aggregation in charged nanoparticles. *Chem. Mat.* **28**, 2348-2355 (2016).
24. Shi, L., Carn, F., Goukassov, A., Buhler, E. & Boué, F. Self-induced crystallization in charged gold nanoparticle-semiflexible biopolyelectrolyte complexes. *Langmuir* **36**, 7925–7932 (2020).
25. Borkowska, M. et al. Targeted crystallization of mixed-charge nanoparticles in lysosomes induces selective death of cancer cells. *Nat. Nanotechnol.* **15**, 331–341 (2020).
26. Zhang, R. et al. Acid-induced in vivo assembly of gold nanoparticles for enhanced photoacoustic imaging-guided photothermal therapy of tumors. *Adv. Healthc. Mater.* **9**, 2000394 (2020).
27. Pillai, P. P., Kowalczyk, B., Pudlo, W. J. & Grzybowski, B. A. Electrostatic titrations reveal surface compositions of mixed, on-nanoparticle monolayers comprising positively and negatively charged ligands. *J. Phys. Chem. C* **120**, 4139–4144 (2016).

28. Schlenoff, J. B., Li, M. & Ly, H. Stability and self-exchange in alkanethiol monolayers. *J. Am. Chem. Soc.* **117**, 12528–12536 (1995).
29. Dong, H. et al. One-pot synthesis of robust core/shell gold nanoparticles. *J. Am. Chem. Soc.* **130**, 12852–12853 (2008).
30. Saha, S., Bruening, M. L. & Baker, G. L. Facile synthesis of thick films of poly(methyl methacrylate), poly(styrene), and poly(vinyl pyridine) from Au surfaces. *ACS Appl. Mater. Interfaces* **3**, 3042–3048 (2011).
31. Liljeström, V., Mikkilä, J. & Kostiainen, M. A. Self-assembly and modular functionalization of three-dimensional crystals from oppositely charged proteins. *Nat. Commun.* **5**, 4445 (2014).
32. Kostiainen, M. A. et al. Electrostatic assembly of binary nanoparticle superlattices using protein cages. *Nat. Nanotechnol.* **8**, 52–56 (2013).
33. Künzle, M., Eckert, T. & Beck, T. Binary protein crystals for the assembly of inorganic nanoparticle superlattices. *J. Am. Chem. Soc.* **138**, 12731–12734 (2016).
34. Gitlin, I., Carbeck, J. D. & Whitesides, G. M. Why are proteins charged? Networks of charge–charge interactions in proteins measured by charge ladders and capillary electrophoresis. *Angew. Chem. Int. Ed.* **45**, 3022–3060 (2006).
35. de Graff, A. M. R., Hazoglou, M. J. & Dill, K. A. Highly Charged Proteins: The Achilles' heel of aging proteomes. *Structure* **24**, 329–336 (2016).
36. Lawrence, M. S., Phillips, K. J. & Liu, D. R. Supercharging proteins can impart unusual resilience. *J. Am. Chem. Soc.* **129**, 10110–10112 (2007).
37. Ma, C., Malessa, A., Boersma, A. J., Liu, K. & Herrmann, A. Supercharged proteins and polypeptides. *Adv. Mater.* **32**, 1905309 (2020).
38. Simon, A. J. et al. Supercharging enables organized assembly of synthetic biomolecules. *Nat. Chem.* **11**, 204–212 (2019).
39. House, J. E. TG study of the kinetics of decomposition of ammonium carbonate and ammonium bicarbonate. *Thermochim. Acta* **40**, 225–233 (1980).
40. Bian, T. et al. Electrostatic co-assembly of nanoparticles with oppositely charged small molecules into static and dynamic superstructures. *Nat. Chem.* **13**, 940–949 (2021).
41. Auyeung, E. et al. DNA-mediated nanoparticle crystallization into Wulff polyhedra. *Nature* **505**, 73–77 (2014).
42. Seo, S. E., Girard, M., de la Cruz, M. O. & Mirkin, C. A. The importance of salt-enhanced electrostatic repulsion in colloidal crystal engineering with DNA. *ACS Central Sci.* **5**, 186–191 (2019).
43. Park, D. J. et al. Plasmonic photonic crystals realized through DNA-programmable assembly. *Proc. Natl. Acad. Sci. USA* **112**, 977–981 (2015).
44. Santos, P. J., Gabrys, P. A., Zornberg, L. Z., Lee, M. S. & Macfarlane, R. J. Macroscopic materials assembled from nanoparticle superlattices. *Nature* **591**, 586–591 (2021).
45. Lewis, D. J., Zornberg, L. Z., Carter, D. J. D. & Macfarlane, R. J. Single-crystal Winterbottom constructions of nanoparticle superlattices. *Nat. Mater.* **19**, 719–724 (2020).
46. Zeng, H., Li, J., Liu, J. P., Wang, Z. L. & Sun, S. Exchange-coupled nanocomposite magnets by nanoparticle self-assembly. *Nature* **420**, 395–398 (2002).
47. Smith, A. M. et al. Quantitative analysis of thiolated ligand exchange on gold nanoparticles monitored by ^{1}H NMR spectroscopy. *Anal. Chem.* **87**, 2771–2778 (2015).
48. Catalan, E. Mémoire sur la théorie des polyèdres. *J. l'École Polytechnique* **41**, 1–71 (1865).
49. Thaner, R. V. et al. The significance of multivalent bonding motifs and "bond order" in DNA-directed nanoparticle crystallization. *J. Am. Chem. Soc.* **138**, 6119–6122 (2016).
50. Wang, M. X. et al. Altering DNA-programmable colloidal crystallization paths by modulating particle repulsion. *Nano Lett.* **17**, 5126–5132 (2017).